Available online at www.sciencedirect.com
SCIENCE DIRECT
Journal of Catalysis 226 (2004) 443–456
JOURNAL OF CATALYSIS
www.elsevier.com/locate/jcat

Effects of the $CePO_4$ on the oxygen storage and release properties of CeO_2 and $Ce_{0.8}Zr_{0.2}O_2$ solid solution

C. Larese [a], F. Cabello Galisteo [a], M. López Granados [a,*], R. Mariscal [a], J.L.G. Fierro [a], P.S. Lambrou [b], A.M. Efstathiou [b]

[a] *Instituto de Catálisis y Petroleoquímica, CSIC, C/ Marie Curie 2, Cantoblanco, 28049 Madrid, Spain*
[b] *Department of Chemistry, University of Cyprus, P.O. Box 20537, CY 1678 Nicosia, Cyprus*

Received 16 March 2004; accepted 8 June 2004

Available online 20 July 2004

Abstract

In an attempt to gain fundamental information about the role of P on the chemical deactivation of a three-way catalyst (TWC), P was deliberatively incorporated in CeO_2 and $Ce_{0.8}Zr_{0.2}O_2$ solid solution. XRD, Raman, XPS, and N_2 physisorption studies have indicated that monazite, a Ce(III) phosphate ($CePO_4$) solid phase, is located at the surface/subsurface region of both solids. Different experimental approaches were used to investigate the alteration by P incorporation of the redox chemistry of CeO_2 and $Ce_{0.8}Zr_{0.2}O_2$ solids that is relevant to the oxygen storage and release properties of the current commercial TWCs. In particular, H_2-TPR, dynamic OSC measurements using CO and H_2 pulses, $^{18}O_2$ temperature-programmed isotopic exchange (TPIE), and $^{18}O_2$ transient isothermal isotopic exchange have been used. These studies revealed that the amount of labile surface and bulk oxygen and the bulk oxygen diffusion rates are significantly reduced when the solids are contaminated with phosphorus. The monazite present in the surface and subsurface region of the solid is proposed to be responsible for these results. The reduction of Ce(IV) present in the CeO_2 and $Ce_{0.8}Zr_{0.2}O_2$ solids is also affected. Ce(III) in monazite is very stable and cannot be oxidized to Ce(IV). Therefore, it cannot participate in the redox Ce(IV)/Ce(III) couple needed for the reduction of Ce(IV). Moreover, the formation of bulk and surface O vacant sites needed for the O storage and release steps involved in the OSC process was also found to be affected. The results of the present work provide support to the hypothesis that formation of monazite is one of the main chemical deactivation mechanisms of real TWCs since $CePO_4$ was found in deactivated vehicle-aged TWCs.

Keywords: TWC deactivation; $CePO_4$; Raman; XPS; TPR; Oxygen isotopic exchange; OSC

1. Introduction

Phosphorus has been established as a common contaminant of vehicle-aged three-way catalysts (TWC) [1–6] that reacts with the active components of the washcoat of TWC. Cerium phosphate ($CePO_4$), a Ce(III) phase, has been detected as one of the phases formed between P and CeO_2, and/or P and $Ce_{1-x}Zr_xO_2$ solid solution present in the washcoat of a vehicle-aged and of a lab-aged TWC [7,8]. Since $CePO_4$ is very stable and it can be neither decomposed nor oxidized [9–12], it has been postulated that it may lock the Ce(III)/Ce(IV) redox couple [7,12]. CeO_2 and $Ce_{1-x}Zr_xO_2$ solid solution have become indispensable oxygen-storage components of the washcoat of TWC due to their large concentration of oxygen-vacant sites, fast exchange of surface oxygen with gas-phase oxygen species, and the high diffusion rates of bulk oxygen toward the surface of these solids. All these important features (named oxygen-storage capacity, OSC) are not found in most of the metal oxides used in various technological applications [13,14]. These features make Ce-based metal oxide mate-

* Corresponding author. Fax: +34-91-5854760.
E-mail address: mlgranados@icp.csic.es (M.L. Granados).

0021-9517/$ – see front matter
doi:10.1016/j.jcat.2004.06.013

rials essential for the correct functioning of TWC during the rapid oscillation of the composition of the exhaust gas around the stoichiometric A/F value. If the Ce(III)/Ce(IV) redox couple becomes locked, the OSC property of the TWC is seriously damaged and the TWC performance is expected to be largely deteriorated.

The amount of OSC in a vehicle-aged catalyst was found to be significantly reduced compared to that in the fresh TWC [12,15] and $CePO_4$ has been detected in those aged catalysts [7,8]. Both effects have also been observed in the aged TWC sample where its catalytic performance was clearly deteriorated [7,12]. It has been suggested that formation of $CePO_4$ is largely responsible for the reduction in the amount of OSC and deactivation of TWC [7,12]. However, a unique relationship between the formation of $CePO_4$ and the failure of good performance of TWC (e.g., decrease of OSC) seems difficult to be made in a straightforward manner for a vehicle-aged TWC. This is because of the number and the complexity of the real phenomena that lead to the deactivation of TWC.

Phosphorus is not the only contaminant deposited and detected in a vehicle-aged TWC that can potentially participate in its deactivation. Ca, Zn, Fe, Pb, and other contaminants were found and characterized as being likely responsible for the deterioration of TWC catalytic performance [3,5,6,16]. The redox properties of cerium oxide and, therefore, its OSC properties can also deteriorate because of the severe thermal aging to which the TWC is subjected under real driving conditions [17,18], and not only because of the formation of $CePO_4$.

The deliberate incorporation of contaminants under controlled conditions to systems with simpler compositions to those experienced in a real TWC seems a reasonable approach in order to reveal the mechanism of TWC deactivation by chemical degradation. Thus, we have initiated a research program toward understanding the real effects that the presence of P could cause in the chemical and structural properties of CeO_2 and $Ce_{1-x}Zr_xO_2$ solid solution. In particular, of interest was to investigate the influence of P on the reducibility of Ce(IV) and the OSC properties of these solid supports. In the present work, phosphorus was deliberately added to CeO_2 and $Ce_{0.8}Zr_{0.2}O_2$ mixed oxides at a P/Ce ratio similar to that detected in vehicle-aged three-way catalysts [7,19] with the intention of forming $CePO_4$. The formation of $CePO_4$ on the surface and in the bulk of these solids was studied by Raman, XPS, XRD, and N_2 physisorption techniques. The effects that P incorporation in CeO_2 and $Ce_{0.8}Zr_{0.2}O_2$ solids could cause on the redox chemistry of these solids were studied by H_2-TPR, OSC measurements (pulse and dynamic experiments), and by ^{18}O isotopic exchange under isothermal and temperature-programmed conditions.

2. Experimental

2.1. Synthesis of CeO_2 and $Ce_xZr_{1-x}O_2$ solids

The CeO_2 and $Ce_xZr_{1-x}O_2$ mixed oxides were prepared by coprecipitation with ammonia of a solution containing the corresponding nitrates, $Ce(NO_3)_3 \cdot 6H_2O$ and $ZrO(NO_3)_2 \cdot xH_2O$. For this purpose, an aqueous solution of NH_4OH (3 N) was prepared and added dropwise to an aqueous solution containing the Ce and Zr salts at the appropriate composition, to yield an atomic ratio of $Ce/Zr = 4$, until a pH 10 was obtained. It is noted that the Zr content in the zirconium salt was determined by chemical analysis. After precipitation, the obtained hydroxide was filtered, extensively washed, and then dried at 383 K for 24 h. The thus obtained solid was then calcined in air at 873 K (heating rate 5 K/min) for 12 h. A fraction of the sample was recalcined for 12 additional hours at 873 K (5 K/min). The solids thus obtained were labeled as Ce and CeZr. The remaining sample was impregnated with phosphorus (P) according to the following procedure. A given amount of $(NH_4)_2HPO_4$ was dissolved in water and the obtained solution was poured in a flask containing the Ce–Zr–O mixed metal oxide to yield an atomic ratio of $P/(Ce + Zr) = 0.2$. Then, the suspension was smoothly stirred for 2 h and the excess water was evaporated in a rotary evaporator (333 K, $P < 0.1$ atm). The P-containing samples were then calcined in air at 873 K (5 K/min) for 12 h and labeled as CeP and CeZrP. It is important to point out that all samples prepared (Ce, CeP, CeZr, and CeZrP) were calcined in air at 873 K for 24 h in two steps of 12 h each. Therefore, differences in the chemical behavior of the solids must be interpreted as due to P incorporation in the solids and not to differences in the calcination procedure applied.

2.2. Characterization of CeO_2 and $Ce_xZr_{1-x}O_2$ solids

2.2.1. X-ray diffraction studies

Powder X-ray diffraction (XRD) patterns were recorded in the 5–85° 2θ range in the scan mode (0.02°, 1 s) using a Seifert 3000 XRD diffractometer equipped with a PW goniometer with Bragg–Brentano $\theta/2\theta$ geometry, an automatic slit, and a bent graphite monochromator. The unit cell parameters were obtained by refining the peak positions of the XRD patterns with a least-squares refinement method after using the program CELREF (CELREF unit-cell refinement software for Windows). For the determination of peak position, the peak profiles were fitted with the commercially available ANALYZE program (pseudo Voigt function).

2.2.2. Raman spectroscopy

Raman spectra were recorded with a Renishaw 1000 spectrophotometer equipped with a cooled (200 K) CCD detector and a holographic Notch filter that removes the elastic scattering. Samples were excited with the 514 nm Ar line.

Spectra acquisition consisted of 5 scans of 60-s duration for each sample. All samples were pretreated in dry air at 523 K (100 (N mL)/min, 30 min) in an in situ cell (Linkam, TS-1500) before the spectra were recorded at 473 K under dry air flow.

2.2.3. X-ray photoelectron spectroscopy

X-ray photoelectron spectroscopy (XPS) studies were performed with a VG Escalab 200 R spectrometer equipped with a hemispherical electron analyzer and an Mg-K_α (1253.6 eV) X-ray source. The sample was first placed in a copper holder mounted on a sample rod in the pretreatment chamber of the spectrometer and then outgassed at room temperature for 1 h before being transferred to the analysis chamber. A certain region of the XPS spectrum was then scanned a number of times in order to obtain a good signal-to-noise ratio. The binding energies (BE) were referenced to the spurious C 1s peak (284.6 eV) used as internal standard to take into account charging effects. The areas of the peaks were computed by fitting the experimental spectra to Gaussian/Lorenztian curves after removal of the background (Shirley function). Surface atomic ratios were calculated from peak area ratios normalized by the corresponding atomic sensitivity factors [20].

2.2.4. BET surface area measurements

Nitrogen adsorption isotherms were recorded at liquid nitrogen temperature (77 K) using a Micromeritics ASAP 2000 apparatus. Prior to determination of an adsorption isotherm, the sample was degassed at 413 K for 12 h.

2.2.5. H_2 temperature-programmed reduction studies

Hydrogen temperature-programmed reduction (TPR) response curves were obtained from a 100-mg sample placed in a U-shaped quartz reactor, the exit of which was connected to a Balzer Prisma quadrupole mass spectrometer (QMS 200) for on-line gas analysis. The sample consisted of solid particles in the 0.42–0.5 mm range. The gas flow rate was 100 (N mL)/min (5% H_2/Ar) and the heating rate was 10 K/min (298–1223 K). The H_2 signal ($m/z = 2$) and the H_2O signal ($m/z = 18$) in the mass spectrometer were continuously monitored in order to follow the kinetics of reduction processes of the solid metal oxides investigated. Gas lines from the reactor to the inlet of the mass spectrometer were heated to 393 K to avoid water condensation. For the quantification of water signal, a calibration curve was obtained by reducing different known amounts of CuO under the same H_2 TPR conditions as those applied in the present samples.

2.2.6. Oxygen-storage capacity measurements

The oxygen-storage capacity (μmol-O/g) of Ce, CeP, CeZr, and CeZrP samples was measured after using the pulse injection method initially developed by Yao et al. [21]. Both H_2 and CO molecular species were used to measure the stored oxygen in the sample. The dynamic OSC amount was also measured during a step-alternating gas concentration switch 1.5% O_2/He → He → 3% CO/3% Ar/He. The transient flow system, the microreactor, and the mass spectrometer used have previously been described [22].

The reactive oxygen species present in the catalyst sample is defined as the amount of CO consumed, in the case that CO (consecutive pulses) is used as a titrating molecular species of oxygen, or the amount of O_2 consumed during the reoxidation stage of the pulse experiment [21,23]. The latter amount of oxygen is referred as the "oxygen-storage capacity complete" (OSCC). The amount of the most reactive oxygen (labile oxygen) of the catalyst is defined as the amount of oxygen species that react during the first CO pulse, and it is called oxygen-storage capacity. The amount of catalyst sample used for the pulse injection experiments was 100 mg in powder form. The general experimental procedure applied for measuring the oxygen-storage capacity by pulse injection experiments was as follows. Initially the catalyst sample was pretreated with a 20% O_2/He gas mixture at a given calcination temperature (T_{osc}) for 1 h (heating rate of 10 K/min from room T to T_{osc}). The reactor was then flushed with He for 5 min at T_{osc} and then cooled to the reaction temperature (T_{rxn}) in He flow. For the OSC measurements, the catalyst sample was reacted with one CO pulse (50 μmol) or one H_2 pulse (50 μmol) and then reoxidized with several successive pulses of O_2 (one oxygen pulse equals 10 μmol) at the same temperature (T_{rxn}). In the case of OSCC measurements, the sample was reacted with several successive pulses of CO or H_2 and then reoxidized with several successive pulses of O_2.

2.2.7. Isotopic $^{18}O_2$-exchange studies

Temperature-programmed isotopic exchange (TPIE) experiments were conducted as follows. After calcination of the fresh sample (100 mg) at 873 K in air for 2 h, the reactor was flushed in He at 873 K for 15 min to remove all oxygen in the gas phase of the reactor and the gas lines. The reactor was then cooled in He flow to 300 K and the feed was switched to a 3 mol% $^{16}O_2$/He gas mixture for 15 min. A switch to the equivalent isotopic 3 mol% $^{18}O_2$/He gas mixture (Isotec, Inc., USA, 97 at% ^{18}O) was then made, while at the same time the temperature of the catalyst was increased to 1073 K at a rate of 30 K/min. All three oxygen isotopic species, namely $^{18}O_2$ ($m/z = 36$), $^{16}O^{18}O$ ($m/z = 34$), and $^{16}O_2$ ($m/z = 32$) were followed continuously with an on-line quadrupole mass spectrometer (Omnistar 300, Balzers).

Transient isothermal ^{18}O-exchange experiments ($T = 873$ K) were also conducted in order to estimate the rate of bulk oxygen diffusion and the diffusivity of bulk oxygen for the various samples investigated. These experiments were designed to probe whether phosphorus is contained in the subsurface/bulk region of the solid. After the sample was treated in the 3 mol% $^{16}O_2$/He gas mixture at 873 K for 2 h, the feed was switched to the equivalent $^{18}O_2$ isotopic gas mixture, while at the same time all three oxygen isotopic species were continuously monitored by on-line mass spec-

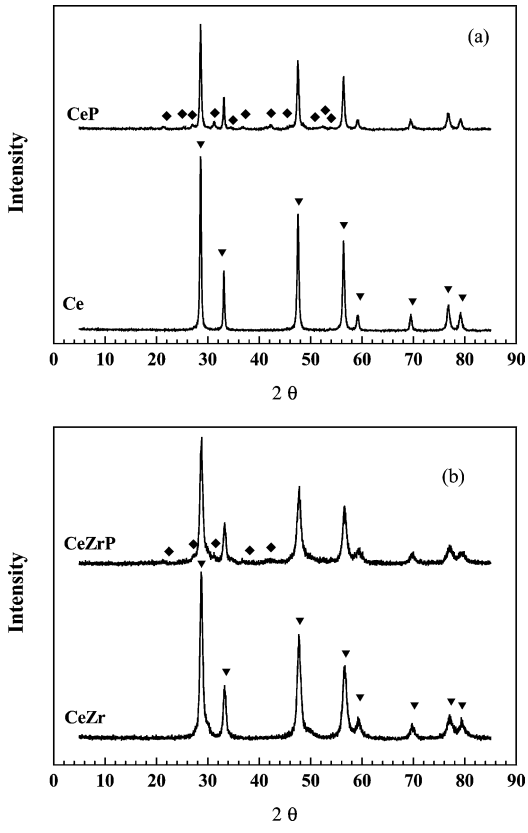

Fig. 1. X-ray diffraction patterns of Ce and CeP samples (a), and of CeZr and CeZrP samples (b).

trometry. The transient gas flow system, the reactor system, and calibration procedures of the mass spectrometer used were previously described [22].

3. Results

3.1. X-ray diffraction studies

Fig. 1a presents the obtained diffractograms of Ce and CeP samples after calcination in air at 873 K. For the Ce sample, reflections due to the cubic CeO_2 fluorite structure are visible (▼). For the CeP solid, reflections due to CeO_2 (fluorite structure) and additional, but much weaker, reflections due to $CePO_4$ (monazite) (◆) could be observed. The XRD pattern of the CeZr sample (Fig. 1b) is quite similar to that of the Ce sample (Fig. 1a). The peaks marked as (▼) arise from the $Ce_xZr_{1-x}O_2$ solid solution. In the region of the $Ce_xZr_{1-x}O_2$ phase diagram (Ce content = 80%), cubic or tetragonal phases with low tetragonality (e.g., c/a very close to 1) can exist [24]. The XRD pattern is not adequate to differentiate between cubic and tetragonal symmetry and Raman characterization is required [25,26]. However, the formation of a $Ce_xZr_{1-x}O_2$ solid solution is confirmed by the fact that the a value contracts with respect to that of Ce sample (from 5.4114 to 5.3981 Å) as reported in Table 1. This is due to the substitution of Ce^{4+} cation by the smaller

Table 1
Structural and textural properties and surface composition of Ce, CeP, CeZr, and CeZrP samples

Solid sample	BET area (m^2/g)	Lattice parameter a (Å), cubic CeO_2	P/Ce atomic ratio, XPS
Ce	12.8	5.4114 ± 0.0002	–
CeP	4.6	5.4122 ± 0.0003	0.71
CeZr	21.7	5.3981 ± 0.0008	–
CeZrP	5.6	5.3991 ± 0.0014	0.89

Zr^{4+} within the CeO_2 lattice. The a value of the solid solution is compared reasonably well with that reported in the literature for a solid solution of similar composition [27,28]. Moreover, it must be stressed that the reflections observed for the mixed oxide are wider (compare Figs. 1a (Ce) and 1b (CeZr)), indicating smaller crystal sizes for this solid. Concerning the CeZrP sample (Fig. 1b), reflections due to the $Ce_xZr_{1-x}O_2$ solid solution are clearly observed, while those belonging to the $CePO_4$ solid phase are of very low intensities, lower than those observed in the CeP sample (compare Figs. 1a and 1b). These results may suggest the presence of very small $CePO_4$ microcrystals, a result that might be expected considering the smaller crystal size of the $Ce_{0.8}Zr_{0.2}O_2$ solid observed compared to that of pure CeO_2.

3.2. Raman spectroscopic studies

Fig. 2 presents Raman spectra related to the effect of P addition in the Ce oxide (Fig. 2a) and $Ce_xZr_{1-x}O_2$ mixed oxide (Fig. 2b) sample. The Raman spectrum of the Ce sample (Fig. 2a) displays a strong band at 462 cm^{-1}, which is assigned to the symmetric breathing mode of the O atoms around each Ce^{4+} cation (Raman mode with F_{2g} symmetry in metal oxides with a fluorite structure) [29]. Other weaker bands observed at 242 and 1170 cm^{-1} were also observed in the Raman spectrum of cubic CeO_2 [30,31], and these are assigned to a second-order scattering effect. The addition of P in CeO_2 solid results in the appearance of new intense Raman bands at 968 and 1054 cm^{-1}. Two shoulders at 990 and 1069 cm^{-1} could also be seen (Fig. 2a). These new bands correspond to the formation of monazite, $CePO_4$ [8].

The Raman spectrum of the CeZr sample (Fig. 2b) is dominated by the strong band recorded at 464 cm^{-1} due to the cubic phase. Moreover, Raman bands assigned to t″ are not visible [25,26,32], while the two weak bands at 252 and 1186 cm^{-1} are assigned to a second-order scattering effect of the cubic phase. The band at 605 cm^{-1} has been reported to be observed with small CeO_2 particles and is related to the presence of bulk oxygen vacancies [30]. The incorporation of P introduces several new features in the CeZrP sample. The new bands observed at 970 and 990 cm^{-1} are assigned to monazite, $CePO_4$ [8], while the other bands appearing are overshadowed by two more intense bands recorded at 1044 and 1121 cm^{-1}. The assignment of these bands is more difficult, although similar bands have been observed when P was added to ZrO_2 [33,34]. The latter bands have been as-

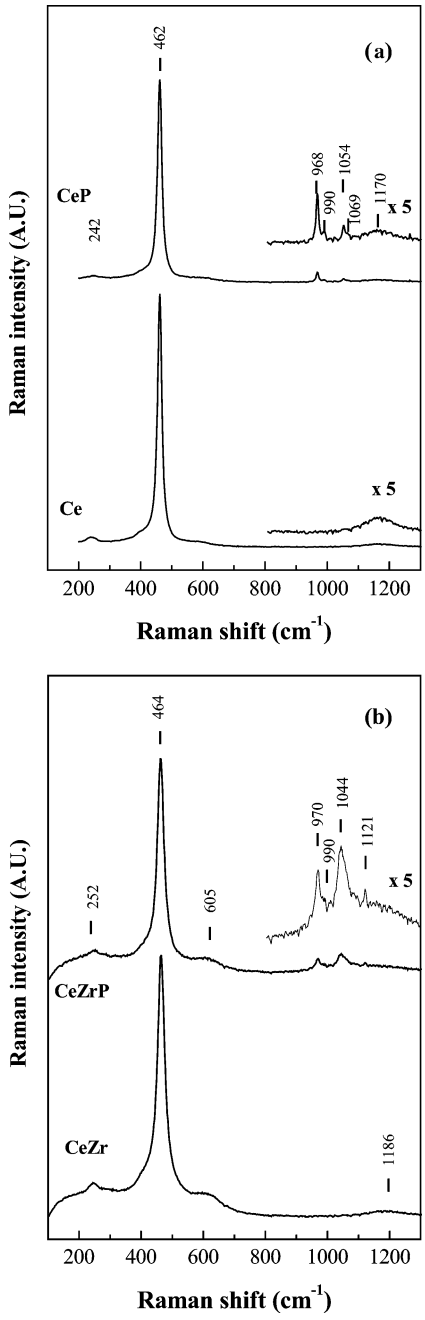

Fig. 2. Raman spectra of Ce and CeP samples (a), and of CeZr and CeZrP samples (b).

signed to ZrP_2O_7 or to phosphate groups anchored on ZrO_2 (ZrO_2PO_2H).

3.3. X-ray photoelectron spectroscopic studies

Fig. 3 presents XPS spectra of the Ce 3d core level for all samples investigated. The XPS spectrum of Ce 3d in Ce(IV) oxides shows six peaks (three pairs of spin–orbit doublets), while Ce(III) oxide exhibits four peaks (two pairs). According to the thoroughly accepted convention as suggested by Burroughs et al. [35], Ce $3d_{3/2}$ multiplets are labeled U,

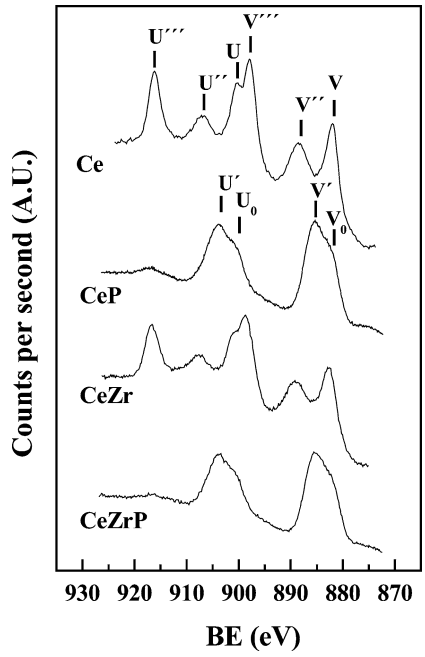

Fig. 3. X-ray photoelectron spectra of Ce 3d core levels of Ce, CeP, CeZr, and CeZrP samples.

whereas those of $3d_{5/2}$ are labeled V. In the case of pure Ce(IV) oxide, V, V″, and V‴ peaks for the Ce $3d_{5/2}$ core level and U, U″, and U‴ peaks for the Ce $3d_{3/2}$ level can be identified in its XPS spectrum (from low to high binding energy). For pure Ce(III) oxide, V_0 and V′ features for the Ce $3d_{5/2}$ core level and U_0 and U′ features for the Ce $3d_{3/2}$ level can be seen. When Ce(IV) and Ce(III) oxidation states coexist in a cerium oxide, up to 10 features can be recognized.

The X-ray photoelectron spectra shown in Fig. 3 can be interpreted according to the comments offered in the previous paragraph. A qualitative estimation of the degree of reduction of Ce(IV) oxide can be made based on the two features of the Ce 3d core level. The first feature is the valley defined by the V and V″ features of the spectrum. If Ce oxide contains only a low amount of Ce(III), the valley is very well defined [36–40]. If the degree of reduction of Ce(IV) to Ce(III) is high, thus Ce(III) becomes more concentrated, the V′ feature of Ce(III) becomes more intense, and the valley between V and V″ starts to vanish. Second, although the relation between the integrated area of the U‴ feature and the Ce(IV) concentration is not linear [36,37,41], the U‴ isolated peak could be taken as a semiquantitative index of the degree of reduction of ceria. A comparison between the area of this Ce(IV) feature and any of the other features can give an estimation of the Ce(III)/Ce(IV) ratio.

The XPS of the Ce 3d level of Ce sample (Fig. 3) shows a typical spectrum of Ce(IV), where little Ce(III) is present. The latter is true because otherwise the U‴ peak should have been much lower and the valley defined between the V and V″ peaks should have been less well defined. On the contrary, the CeP sample exhibits a typical XP spectrum

of the Ce(III) 3d core level, implying that Ce(III) predominates at the surface of the sample. Only a little amount of Ce(IV) is present according to the low intensity of the peak at 916.5 eV (the U‴ feature of Ce(IV) 3d core level). The P/Ce atomic ratio in the CeP and CeZrP samples was calculated and it is found to be 0.71 and 0.89, respectively (see Table 1). These values are much higher than the value of 0.2 and 0.25 expected for the bulk P/Ce ratio of CeP and CeZrP solids, respectively. This result strongly suggests that P is mainly concentrated at the surface and a few atomic layers in the subsurface region. It is also very likely that P is spread over the surface and it is accumulated at the surface of the grains of Ce and CeZr metal oxides. The Ce(III) detected by XPS must be assigned to the $CePO_4$ phase in harmony to what was found in the Raman spectroscopy (Fig. 2) and XRD (Fig. 1) studies. In fact, the P/Ce ratio detected by XPS is close to 1, which is the ratio corresponding to $CePO_4$. The latter is a very stable phase that cannot be decomposed or transformed even under high calcination temperatures [9–11]. The Ce(III) detected in the CeP sample by XPS is not oxidized to Ce(IV) during calcination. Therefore, the assignment of this Ce(III) to $CePO_4$ seems very reasonable.

The XPS spectrum of Ce 3d core levels for the CeZr sample is very similar to that obtained for the Ce sample. In this case, according to the slightly relative lower intensity of the U‴ peak and the ill-defined valley between V and V″ features, it seems that slightly more Ce(III) is present in the CeZr sample, although the Ce(IV) still predominates. For the CeZrP sample, the XPS features indicate a very large proportion of Ce(III) at the surface of the solid and a very small proportion of Ce(IV) according to the very low intensity of the U‴ feature. This is in harmony with the detection of $CePO_4$ by XRD and Raman spectroscopies (Figs. 1 and 2).

The amount of Ce(III) detected by XPS on the "surface" of the P-containing samples is remarkably high, where only a minor amount of Ce(IV) is present. It must be stated that Ce(III) could be detected by XPS in Ce oxides because of the high vacuum applied or due to photoreduction processes. However, it is not likely that a high proportion of Ce(III) in the CeP and CeZrP samples can be formed by this photoreduction process. A previous reduction treatment at high temperatures should have been required in order to obtain the clear XPS Ce(III) pattern that has been recorded in the CeP and CeZrP samples. In the present work, all samples investigated were calcined in air at 873 K for 12 h and no prereduction step has been carried out in the XPS equipment. Therefore, the high stability of the Ce(III) formed at the surface of the samples after P addition that cannot be oxidized even after the very intense calcination treatment applied is due to the formation of $CePO_4$, in harmony with the well-documented stability of this phase under severe oxidizing treatments [9–11].

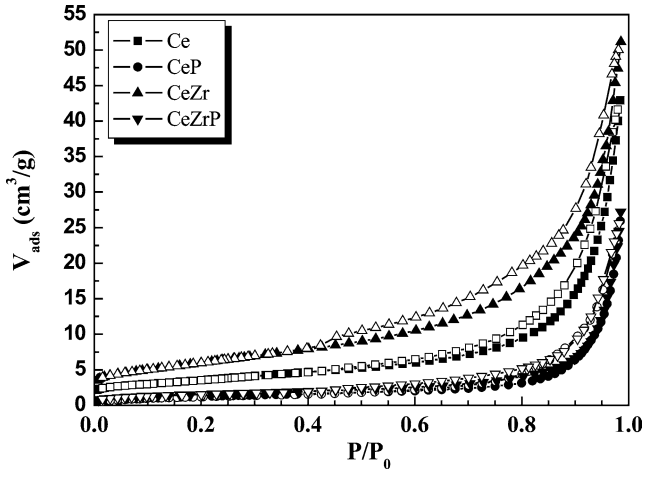

Fig. 4. N_2 adsorption/desorption isotherms ($T = 77$ K) obtained over the Ce, CeP, CeZr, and CeZrP samples.

3.4. Surface area measurements

Fig. 4 shows N_2 adsorption isotherms for the samples studied in the present work. A perusal of the isotherms clearly demonstrates that incorporation of P in the Ce and CeZr samples results in a modification of their surface texture. Although the type of the isotherm and its hysteresis loop do not change by P addition, the amount of N_2 adsorbed is significantly reduced because of the decrease of the specific surface area (see Table 1). This decrease is more intense for the CeZr sample but both CeP and CeZrP phosphated samples displayed similar specific surface areas and isotherms. It is noted that according to the BDDT classification [42], the isotherms presented in Fig. 4 are of type IV and show a hysteresis loop of type H3 due to the existence of interparticle mesoporosity.

3.5. Temperature-programmed reduction studies

In an attempt to gather information about how the presence of $CePO_4$ in the CeP and CeZrP samples affects the reducibility of Ce(IV) to Ce(III), the H_2-TPR traces of all samples were investigated by using on-line mass spectrometry. Figs. 5a and 5b present the TPR transient response curves of water formation from the hydrogen reduction of the samples. According to the reduction mechanism of Ce oxides reported in the literature [43–45], reduction starts with H activation and formation of new OH groups at the surface of the oxide (reversible reduction). Then, it proceeds with slower processes, such as water formation and desorption that are accompanied by Ce(IV) reduction to Ce(III) and formation of an oxygen vacancy (irreversible reduction). Based on this information, it is expected that H_2O evolution will lag behind the H_2 response curve in the TPR spectrum. Therefore, H_2O evolution is in principle a better probe for tracing only the irreversible reduction step. Moreover, the signal-to-noise ratio of the H_2^+ fragment is lower than that of H_2O^+ due to the higher background level of $m/z = 2$ than $m/z = 18$

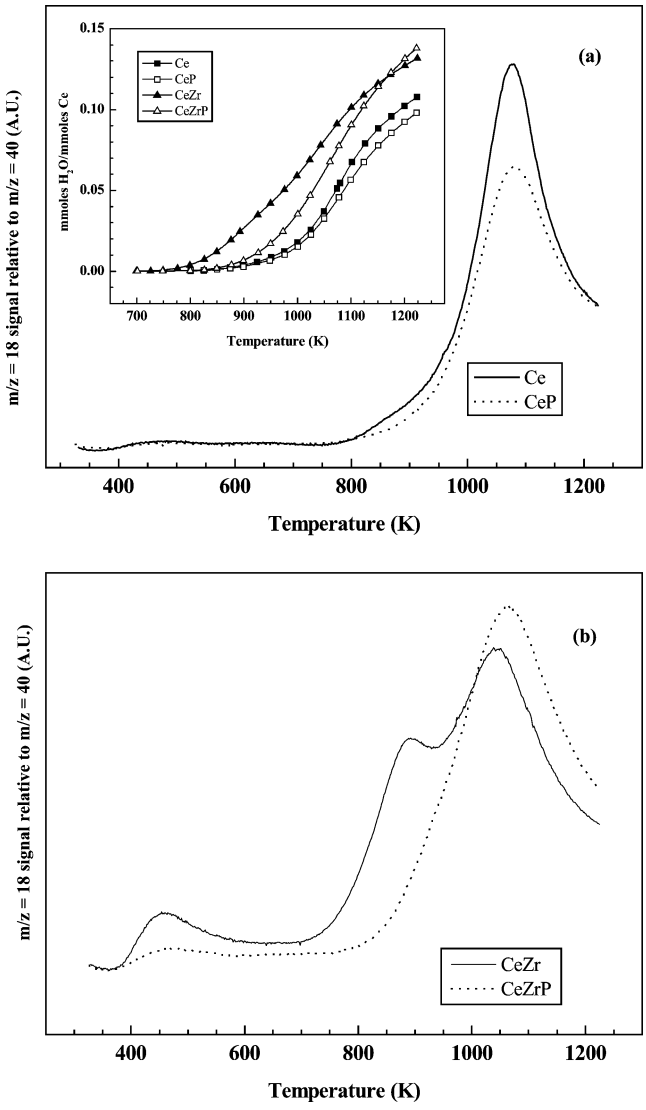

Fig. 5. Transient response of water obtained by on-line mass spectrometry during a H_2 temperature-programmed reduction (TPR) experiment over the Ce and CeP (a), and CeZr and CeZrP (b) samples. Inset in Fig. 5a presents the amount of H_2O (mmol/mmol Ce) produced as a function of reduction temperature during the H_2 TPR experiments.

signal in the MS vacuum chamber [12]. Therefore, the measurements were based on water signal even though the H_2 consumption was also monitored ($m/z = 2$ signal). In fact, it was verified that H_2 consumption and H_2O evolution occur practically simultaneously (a weak shift to lower temperatures (10–20 K) was observed in the H_2 trace). Therefore, readsorption of H_2O is not important in the present experiments.

Fig. 5b clearly illustrates that the TPR transient response curve of water for the CeZr sample is affected by the P incorporation in the sample. First, it can be seen that the H_2O peak at 430 K is much weaker in the CeZrP than the CeZr sample. The lower intensity of this water peak in the phosphated CeZr sample is a consequence of the depletion of very labile oxygen species from the surface of the CeZrP sample. Second, the peak at 890 K in the CeZr solid, which represents a rather surface and subsurface reduction process, is not present in the CeZrP sample. Finally, the reduction process occurring at higher temperatures and represented by the appearance of a peak at 1044 K in the CeZr sample shifts to even higher temperatures ($T_M = 1061$ K) in the CeZrP sample. These features seen in the H_2 TPR response curves of CeZr and CeZrP solids are not seen in the Ce and CeP solid samples (see Fig. 5a).

The inset in Fig. 5a presents the calculated amount (mmol) of H_2O evolved per millimole of Ce present in the sample as a function of reduction temperature for the H_2 TPR experiments. This is more precise information to account for the reduction of Ce since these results reflect the amount of Ce(IV) that is reduced to Ce(III) in the sample. It should be noted that the addition of P (and Zr) in CeO_2 results in a dilution of Ce present in the sample, and thus of the reducible species. As clearly shown, reduction of the CeZr sample occurs at lower temperatures and with higher rates compared to that of the Ce sample. These results agree very well with what has been reported in the literature about the ease of reducibility of Ce(IV) in $Ce_{1-x}Zr_xO_2$ solid solutions [27,45]. Addition of P to the Ce sample (CeO_2) results in a small inhibition of the reducibility of Ce(IV) more evident at higher temperatures. Note that the amount of Ce(IV) reduced in the Ce sample at 1223 K is about 21.5% of the total amount of Ce in the sample. This result is in good agreement with other CeO_2 solids investigated [45]. In the case of the CeP sample, the amount of Ce(IV) reduced at 1223 K is found to be 19.6% which is 10% less than that found in the Ce sample. Therefore, the quantitative changes expressed per millimole of Ce in the original sample are not that large. On the other hand, the effect of P addition in the CeZr solid solution is larger than that observed in the Ce sample, especially in the 750–1100 K range. At higher reduction temperatures both curves converge (Fig. 5b). It is found that the amount of Ce(IV) that is reduced at 975 K in the CeZrP sample is about 42% lower than that obtained in the CeZr sample.

3.6. Oxygen-storage capacity measurements

Fig. 6 presents results of OSC and OSCC measurements (μmol-O/g_{cat}) conducted at $T_{osc} = 773$ K and $T_{rxn} = 773$ K using H_2 and O_2 pulses over Ce, CeP, CeZr, and CeZrP solids according to the experimental procedure given in section 2.2.8. CeO_2 (Ce) and $Ce_xZr_{1-x}O_2$ (CeZr) solids after addition of phosphorus show a dramatic decrease in their ability to store and release oxygen from their surface. However, in terms of percentage reduction in oxygen-storage capacity, CeZr exhibits the highest percentage. More precisely, the Ce sample shows 77% reduction, while CeZr shows a 97.2% reduction in their corresponding OSCC quantity.

Fig. 7 presents results of OSC and OSCC measurements (μmol-O/g_{cat}) conducted after using CO pulses at $T_{rxn} =$ 773 K in a similar way as with H_2 pulses (Fig. 6). It is

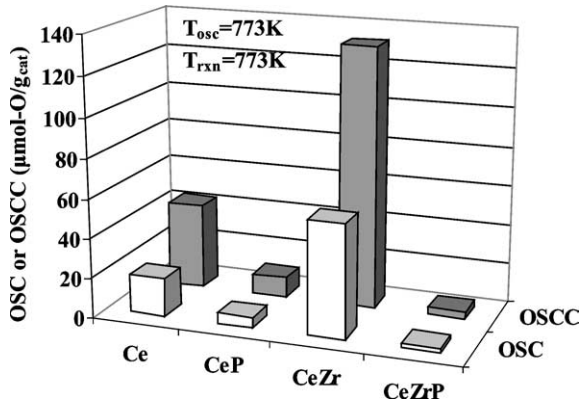

Fig. 6. OSC or OSCC (µmol-O/g) measured by H_2 pulses over Ce, CeP, CeZr, and CeZrP samples. Oxygen pretreatment temperature, $T_{osc} = 773$ K; titration temperature, $T_{rxn} = 773$ K.

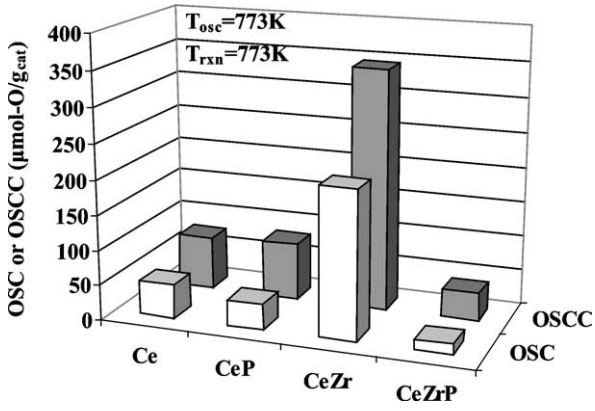

Fig. 7. OSC or OSCC (µmol-O/g) measured by CO pulses over Ce, CeP, CeZr, and CeZrP samples. Oxygen pretreatment temperature, $T_{osc} = 773$ K; titration temperature, $T_{rxn} = 773$ K.

noted that oxygen was previously stored in the sample at $T_{osc} = 773$ K. The amount of oxygen consumed following reoxidation of the sample after CO pulsing is found to be higher than the equivalent amount after H_2 pulsing for all solids investigated. This difference is due to the different transient rates of CO and H_2 oxidation to form CO_2 and H_2O, respectively, which are determined by the different kinetics of CO and H_2 oxidation for the same catalyst surface. On the other hand, the presence of phosphorus in the solid significantly affected the amount of labile oxygen reacted off by CO. Similar results were obtained with hydrogen pulses (Fig. 6).

The present OSC measurements in terms of µmol-O/g after using the H_2 and CO pulse technique (Figs. 6 and 7) are in good agreement with other studies conducted on CeO_2 and $Ce_{1-x}Zr_xO_2$ solid solutions [18,46–48]. In the case of using H_2 as the reducing agent, the ratio of OSCC measured in $Ce_{0.8}Zr_{0.2}O_2$ to that in CeO_2 is found to be about 3.0 ($T_{osc} = 773$ K, $T_{rxn} = 773$ K). These results confirm the significant improvement of oxygen-storage capacity of $Ce_{0.8}Zr_{0.2}O_2$ solid solution compared to pure CeO_2. It is important to note here that for the CeZr sample (Fig. 6)

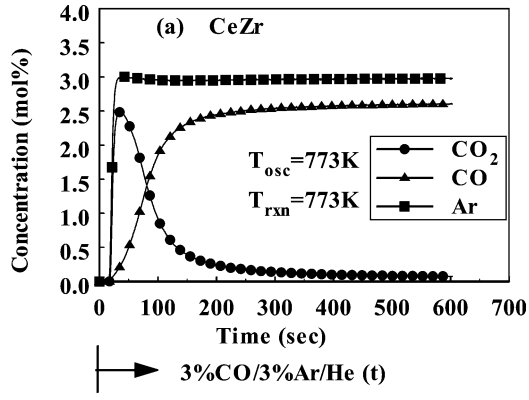

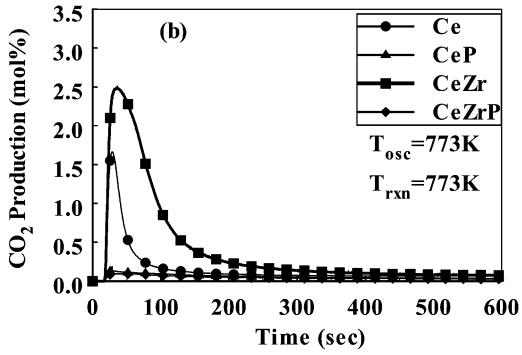

Fig. 8. (a) Transient response curves of Ar, CO and CO_2 obtained during the switch 1.5% O_2/He (1 h, T_{osc}) → He (T_{osc}, 5 min) → 3% CO/3% Ar/He (T_{rxn}, t) over the CeZr sample for measuring the dynamic OSC. $T_{osc} = 773$ K; $T_{rxn} = 773$ K. (b) Transient response curves of CO_2 obtained according to the gas delivery sequence described in (a) for $T_{rxn} = 773$ K and $T_{osc} = 773$ K over the Ce, CeP, CeZr, and CeZrP samples.

the equivalent number of oxygen monolayers that correspond to the OSCC amount is found to be 0.27. This quantity was estimated based on the theoretical number of surface oxygen atoms for ceria (cubic, 13.1 atoms/nm^2) and $Ce_{0.68}Zr_{0.32}O_2$ (cubic, 13.5 atoms/nm^2) reported in the literature [49]. It is noted that the theoretical number of surface oxygen atoms (atoms-O/nm^2) differs by no more than 1.5% for $Ce_xZr_{1-x}O_2$ ($x > 0.5$) in either cubic or tetragonal crystal structures. Thus, the results of Figs. 6 and 7 represent only surface labile oxygen species.

Fig. 8a presents transient isothermal response curves of CO, CO_2, and Ar obtained following the switch 1.5% O_2/He (1 h, T_{osc}) → He (T_{osc}, 5 min) → 3% CO/3% Ar/He (T_{rxn}, t) over the CeZr sample for $T_{osc} = 773$ K and $T_{rxn} = 773$ K in order to measure the dynamic OSC quantity. The area difference between the Ar and CO response curves allows estimation of the amount of CO consumed. Integration of the CO_2 response curve provides the amount of CO_2 formed. A difference in the amount of CO consumed and CO_2 produced suggests that other side reactions must occur [23], as discussed below.

Fig. 8b compares the transient response curves of CO_2 obtained in all four Ce, CeP, CeZr, and CeZrP samples following the same experiment as in Fig. 8a. It is clearly ob-

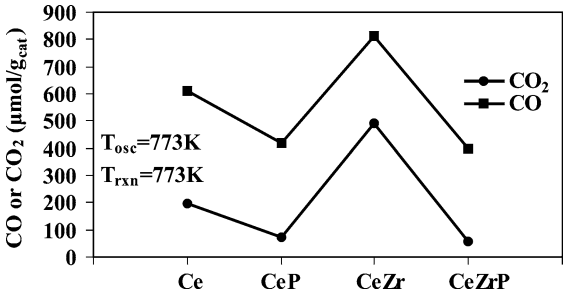

Fig. 9. Amount (μmol/g) of CO and CO_2 consumed and produced, respectively, during the experiment for measuring the dynamic OSC as described in Fig. 8 over the Ce, CeP, CeZr, and CeZrP samples. $T_{osc} = 773$ K, $T_{rxn} = 773$ K.

served that the presence of phosphorus in the solid significantly affects the initial rate of reaction (sudden increase in CO_2 production) between the surface labile oxygen and CO to form CO_2. This result is in harmony with the OSC results obtained after applying the CO pulse technique (see Fig. 7). In the experiments to be described next, it will be shown that the presence of phosphorus affects also to a significant extent the rate of bulk oxygen diffusion toward the surface of the solid.

Fig. 9 compares the amounts of CO consumed and CO_2 produced in the dynamic OSC experiments presented in Fig. 8 after 10 min in 3% CO/3% Ar/He gas mixture. These results clearly illustrate that the interaction of CO with the surface of the solids during the 10-min reaction period leads not only to the $CO + O_s \rightarrow CO_2$ reaction (O_s refers to a surface lattice oxygen atom) but also to other side reactions. These are: (a) the CO_2 chemisorption; (b) the dissociation of CO to give C_s and CO_2 (Boudouard reaction: $2CO_{(g)} \rightarrow CO_{2(g)} + C_s$); and (c) the reaction of CO with –OH surface groups to produce H_2 and CO_2. The latter reaction is based on the observed H_2 signal during the transient experiment. The existence of a 35–90% difference between the amounts of CO_2 produced and CO consumed (see Fig. 9) justifies the above-referenced side-reaction routes.

3.7. $^{18}O_2$ isotopic exchange studies

Fig. 10a presents the transient response curves of $^{16}O_2$ ($m/z = 32$) and $^{16}O^{18}O$ ($m/z = 34$) gaseous oxygen isotopic species obtained during the TPIE experiment described in Section 2.2.7 over Ce and CeP samples, and Fig. 10b over CeZr and CeZrP samples. For CeP and CeZrP samples, the rates of ^{18}O exchange with the surface of the solids are reduced significantly with respect to the uncontaminated-with-phosphorus respective samples. There is a clear shift to higher temperatures in the appearance of a peak maximum of the $^{16}O_2$ TPIE response curve obtained after contamination of the sample with phosphorus. This shift may reflect the increase in activation energy of the bulk oxygen diffusion process. As will be discussed later, the $^{16}O_2$ signal arises from the multiple heteroexchange mechanism of $^{18}O_2(g)$ with the metal oxide solid surface.

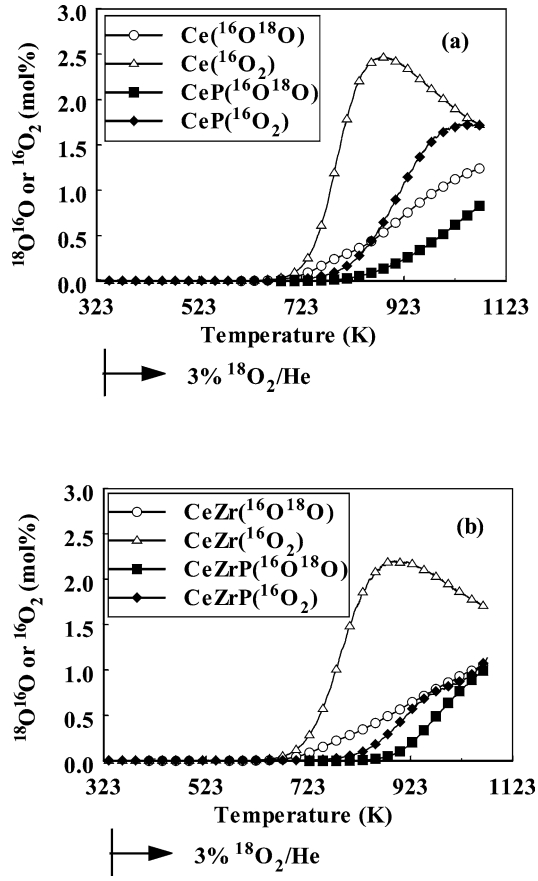

Fig. 10. Transient gaseous responses of $^{16}O_2$ and $^{16}O^{18}O$ isotopic species obtained during a temperature-programmed isotopic exchange (TPIE) experiment according to the following gas delivery sequence: Air (873 K, 2 h) → He (873 K, 15 min) → cool down in He flow to 300 K → 3% O_2/He (300 K, 15 min) → 3% $^{18}O_2$/He (t), T is increased to 1073 K ($\beta = 30$ K/min) over (a) Ce and CeP samples and (b) CeZr and CeZrP samples.

Table 2
Amount (μmol-O/g) and equivalent number of monolayers of ^{16}O exchanged during the TPIE experiment presented in Fig. 10

Solid sample code	Temperature (K)							
	773		873		973		1073	
Ce	0.9[a]	256.6[b]	7.2	2001.6	15.1	4204.5	22.2	6195.9
CeP	0.4	41.4	2.5	252.6	11.9	1189.0	27.6	2763.9
CeZr	0.9	448.0	4.5	2156.9	8.7	4159.3	12.5	6013.9
CeZrP	0.2	27.1	0.9	116.9	5.2	638.1	13.7	1693.0

[a] Values in first column at each temperature represent equivalent number of monolayers of exchangeable oxygen ^{16}O.

[b] Values in second column at each temperature represent amount (μmol-O/g) of exchangeable oxygen in the form of $^{16}O_2 + {}^{16}O^{18}O$.

Table 2 reports the number of equivalent monolayers of atomic oxygen species exchanged during the TPIE experiment (Fig. 10) for all four investigated solids. As clearly illustrated in Table 2, at $T \geqslant 873$ K several monolayers of oxygen had been exchanged with $^{18}O_2(g)$ indicating that, beyond this T, diffusion of O from the inner bulk of the solid is the predominant process of supplying oxygen to the surface.

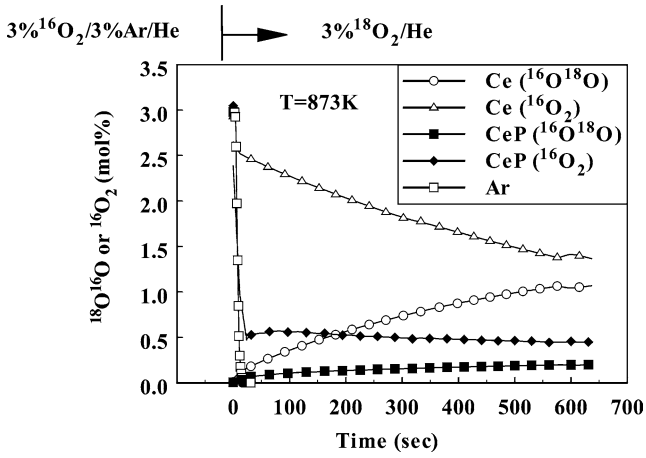

Fig. 11. Transient isothermal exchange experiment performed at 873 K over Ce and CeP samples according to the gas delivery sequence: 3% $^{16}O_2$/He (873 K, 2 h) → 3% $^{18}O_2$/He (873 K, t).

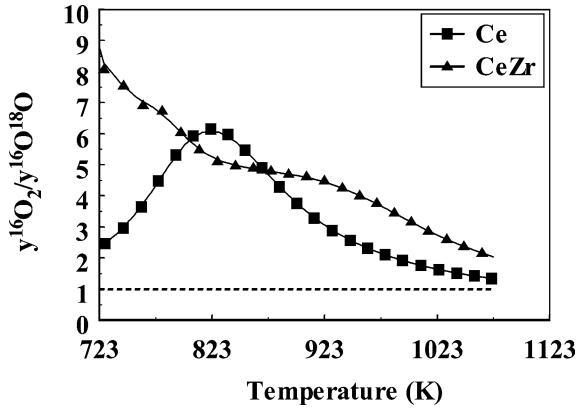

Fig. 12. Discrimination between simple and multiple heteroexchange mechanisms of oxygen over CeO_2 and $Ce_{0.8}Zr_{0.2}O_2$ solids as a function of reaction temperature during the TPIE experiment of Fig. 10. Values of the $y^{16}O_2/y^{16}O^{18}O$ ratio much larger than unity indicate a multiple hetero-exchange mechanism.

Therefore, it is worth noting that the TPIE results show a significant suppression in the amount of exchangeable oxygen (both surface and bulk) in the case of P-contaminated samples. In the case of dynamic OSC measurements (Figs. 8 and 9), the equivalent number of oxygen monolayers for the CeZr sample at the reaction temperature of 773 K is found to be about 1.1 (based on the CO_2 production).

Fig. 11 presents transient isothermal response curves of $^{16}O_2$ ($m/z = 32$) and $^{16}O^{18}O$ ($m/z = 34$) isotopic species following the switch 3% $^{16}O_2$/He (2 h) → 3% $^{18}O_2$/He (t) at 873 K over the Ce and CeP samples. According to Boreskov [50] and Klier et al. [51], two types of oxygen-exchange mechanisms could occur on a solid metal oxide with the real participation of the latter: (a) *simple hetero-exchange* that occurs with the participation of *only one oxygen atom* of the oxide at each of the following steps,

$$^{18}O^{18}O(g) + {}^{16}O_s \Leftrightarrow {}^{18}O^{16}O(g) + {}^{18}O_s, \quad (1)$$

$$^{18}O^{16}O(g) + {}^{16}O_s \Leftrightarrow {}^{16}O_2(g) + {}^{18}O_s, \quad (2)$$

and (b) *multiple hetero-exchange* that occurs with the participation of *two oxygen atoms of the oxide* at each of the following steps:

$$^{18}O^{18}O(g) + 2{}^{16}O_s \Leftrightarrow {}^{16}O_2(g) + 2{}^{18}O_s, \quad (3)$$

$$^{18}O^{16}O(g) + 2{}^{16}O_s \Leftrightarrow {}^{16}O_2(g) + {}^{16}O_s + {}^{18}O_s, \quad (4)$$

$$^{18}O^{16}O(g) + 2{}^{18}O_s \Leftrightarrow {}^{18}O_2(g) + {}^{16}O_s + {}^{18}O_s. \quad (5)$$

The kind of isotopic exchange mechanism, simple vs multiple hetero-exchange, can be differentiated at the beginning of the reaction by the prior appearance in the gas phase of $^{18}O^{16}O$ or $^{16}O_2$, respectively.

From the TPIE experiments presented in Fig. 10, the ratio of $^{16}O_2$ mole fraction to that of $^{16}O^{18}O$ vs temperature is presented in Fig. 12. It is clearly illustrated that at the lowest temperature of 723 K, where oxygen isotopic exchange can be activated and measured, multiple hetero-exchange prevails over the present CeO_2 and $Ce_xZr_{1-x}O_2$ solids. This result is in harmony with that obtained by Duprez and coworkers [49,52,53] after conducting similar experiments but using a batch-recycled rather than a once-through-flow microreactor as in the present work. The latter authors have demonstrated by using FTIR that superoxide (O_2^-) species are populated on the presently investigated Ce and CeZr solids and can exchange with gaseous $^{18}O_2$ via the "place-exchange" mechanism, the latter being one of the two possible pathways of the multiple hetero-exchange mechanism [54–56].

As the temperature in the TPIE experiment increases, simple hetero-exchange also becomes important, and participation of $^{16}O^{18}O$ via either a simple [Eq. (2)] or a multiple [Eq. (4)] hetero-exchange mechanism to yield $^{16}O_2$ makes the interpretation of which mechanism prevails uncertain. Based on the isothermal oxygen isotopic exchange experiments conducted at 873 K (Fig. 11), upon the switch to the isotopic mixture it becomes clear that multiple hetero-exchange prevails. Based on this result and the TPIE results in the 723–823 K range (Fig. 12), it seems that the latter exchange mechanism must prevail at least in the 723–873 K range.

Fig. 11 shows that the rate of $^{16}O^{18}O$ production is significantly higher in the Ce sample compared to that in the contaminated one, CeP. Moreover, the $^{16}O_2$ signal ($m/z = 32$) in the Ce sample does not abruptly fall but it follows a smooth decrease indicating that, at the beginning, surface exchange with $^{16}O_s$ takes place. Later on, when surface $^{16}O_s$ is spent, bulk $^{16}O_b$ progressively participates to a greater extent. In the case of CeP sample, the $m/z = 32$ signal falls steeply indicating that the surface O exchange is remarkably suppressed by the P contamination; note that the BET area of Ce sample is about 3 times larger than that of CeP one.

After about 10 min on the isotopic $^{18}O_2$/He gas mixture, a pseudo-steady state was about to be reached for the $^{16}O^{18}O(g)$ continuous production. This ^{16}O species arises now from the subsurfaced/bulk of the solid. Based on the

analysis reported in the literature [57] for a similar isotopic experiment, the effective diffusion coefficient (D_{eff}) of bulk oxygen diffusion within the crystal lattice of the solid can be estimated from the pseudosteady state rate production of $^{16}O^{18}O$ at time equal to $t_{\text{s.s.}}$. This is given by the following relationship [57],

$$D_{\text{eff}} = \pi t_{\text{s.s.}} (N_A / C_{A0})^2, \quad (6)$$

where N_A (mol/(cm^2 s)) is the flux of atomic oxygen from the bulk to the solid surface, and C_{A0} (mol/cm^3) is the initial concentration of atomic oxygen in the bulk. N_A is calculated by multiplying the $y_{^{16}O^{18}O}$ (mole fraction of $^{16}O^{18}O$(g)) by the total molar flow rate (mol/s) and dividing by the catalyst weight (g) and surface area (cm^2/g). Since the accuracy of the value of D_{eff} depends on the value of $t_{\text{s.s.}}$ for which pseudo-steady state is assumed, for comparison purposes the present work reports an approximate value of the ratio of the bulk diffusion coefficients estimated for the noncontaminated and P-contaminated solids. This ratio was found to be 4.0 at 873 K. In these calculations, the ratio of corresponding values of C_{A0} for each of the two solids (Ce and CeP) was assumed to be about unity. In other words, the amount of P present in the subsurface/bulk of the crystal of CeP does not affect significantly the initial oxygen concentration in the Ce sample. On the other hand, assuming that the latter is not true and after allowing a 20% decrease in the value of C_{A0}, a ratio of 2.6 for the two diffusivity values is obtained. Based on similar experiments performed on CeZr and CeZrP solids, a ratio of 2.8 was estimated (C_{A0} is considered to be the same for the CeZr and CeZrP samples).

The results presented in the previous paragraph (Fig. 11) have clearly demonstrated that phosphorus is present in the subsurface/bulk of CeO_2 and $Ce_{0.8}Zr_{0.2}O_2$ solids, remarkably suppressing the specific rate (mol/(cm^2 s)) of bulk oxygen diffusion.

4. Discussion

One of the key important aspects of this work was to provide experimental evidence about the intrinsic effects that phosphorus deposition on CeO_2 and $Ce_xZr_{1-x}O_2$ solid solution has on their redox properties. In order to correctly address this issue, it is very important to understand first where phosphorus is located in the aforementioned solids after its deposition and calcination in air at 873 K for 12 h.

The similarity of the N_2 isotherms and of the specific surface area of the CeP and CeZrP samples may indicate that the surface texture is influenced by the same surface phase, that of $CePO_4$ detected by Raman and XPS techniques. For the latter case, the surface P/Ce atomic ratio detected by XPS (see Table 1) was close to that of monazite, while Ce(III) predominates at the surface of the samples. It could be argued that $CePO_4$ might spread over part of the initial solid surface causing also reaggregation of the crystallites of the solid affected, thus altering the pore

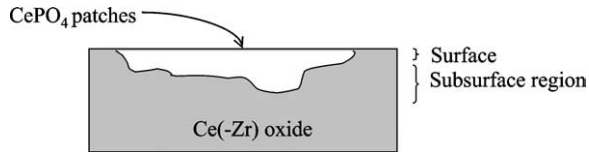

Scheme 1. Pictorial presentation of $CePO_4$ location in Ce and CeZr solids.

structure of both Ce and CeZr solids. A picture that could emerge from the present bulk and surface characterization techniques used is that the incorporated P reacts with the Ce(–Zr) oxide, and as a result of this $CePO_4$ predominates at the surface/subsurface of the resulting material. Scheme 1 depicts this view.

The fact that monazite is detected by XRD and Raman indicates that the sizes of its crystals are large enough to reach the inner bulk of the solid. Although the XPS and Raman characterization results indicate that Ce phosphate predominates at the "surface", they do not allow discarding neither that the surface of the phosphated solids is fully covered by Ce phosphate nor that a fraction of the incorporated P migrates deeper in the bulk. The H_2 TPR, OSC, and $^{18}O_2$ isotopic exchange experiments should be interpreted taking into account what is depicted in Scheme 1. It must also pointed out that the physicochemical processes involved in these experiments are of special concern for the redox chemistry occurred in TWCs, namely reduction of Ce(IV) to Ce(III), formation of O-vacant sites at the surface and in the bulk, and surface and bulk O diffusion.

Regarding the temperature-programmed isotopic $^{18}O_2$ exchange (TPIE, Fig. 10) and the transient isothermal $^{18}O_2$ exchange experiments (Fig. 11), they provide strong evidence that the initial deposition of phosphorus on the surface of ceria and $Ce_xZr_{1-x}O_2$ solids resulted in a large reduction in the rate of surface and bulk oxygen diffusion. This is due to a reduction in the effective diffusivity values of surface and bulk oxygen diffusion processes as outlined under Results. It is proposed that this effect must be related to the presence of $CePO_4$ within the initial crystal structure of ceria and $Ce_xZr_{1-x}O_2$ solids. The relatively large shift toward higher temperatures (more than 150 K) of the peak maximum position (T_M) of the $^{16}O^{16}O$ transient response curve in the TPIE experiments (Fig. 10) in the case of CeP and CeZrP compared to Ce and CeZr solids suggests an increase in the apparent activation energy of the oxygen-exchange process. At temperatures higher than 873 K, it is expected that the overall rate of the exchange process is determined by the rate of bulk oxygen diffusion to the surface [52]. In fact, this is indicated by the number of oxygen monolayers estimated at 873 K (Table 2). It can be argued that the observed shift in T_M cannot be explained by the expected decrease in the initial concentration of bulk oxygen in the CeP and CeZrP solids that diffuse toward the surface. In fact, the high temperature reduction peak observed over a series of $Ce_xZr_{1-x}O_2$ and doped (La^{3+}, Y^{3+}) solid solutions exhibits a T_M value that does not differ by more than 50–60 K in all solid compositions studied of varying degrees of bulk

oxygen concentration [58]. In addition, a very small shift in the peak maximum position of the high-temperature TPR peak is obtained in the H_2 TPR spectra of Figs. 5a and 5b, where a significant decrease in the amount of labile oxygen species in CeP and CeZrP solids is observed.

The number of equivalent monolayers of atomic oxygen species that were exchanged during the TPIE experiment (Fig. 10) and which is reported in Table 2 must be considered as an upper limit given the stoichiometry of exchange reactions [Eqs. (1)–(5)] and that in these calculations the $^{16}O_2$ response was considered as arising from two surface oxygen species ($^{16}O_s$). Also, for the CeP and CeZrP samples the fact that part of the surface of these crystals is covered by $CePO_4$, the exchangeable oxygen species then arise from deeper layers than what is reported in Table 2.

Concerning the OSC measurements, it has been reported [59] that the higher ability of $Ce_xZr_{1-x}O_2$ solids for oxygen storage, as evidenced also in the present work (Figs. 6–9), is related to the higher concentration of oxygen vacancies (ionic defects) at the surface of the solid. In fact, the stabilization at or near the surface of such defects could result in an enhanced ability to activate oxygen as superoxide. This species could then be seen as the "initiator" of the whole storage process [53], where superoxide (O_2^-) species are dissociated into oxygen ions (O^-, O^{2-}) before their migration into the bulk [60]. Therefore, the initial concentration of oxygen precursor species, like O_2^-, plays a significant role in the final measured OSC quantity. The efficiency in the storage of oxygen process would then be directly related to the concentration of oxygen vacancies at the gas/solid interface. These ideas are supported by the present OSC results shown in Figs. 6, 7, and 9, where a larger reduction percentage in the quantity of OSC in phosphated samples is obtained for CeZr than for Ce solid. The presence of surface $CePO_4$ seems to result to a large extent in the reduction of the initial concentration of superoxide species formed during the OSC measurements; $CePO_4$ is unable to be reduced or oxidized, which makes very unlikely the formation of vacant sites.

The TPR technique was also used in this work to study the redox chemistry of phosphated samples. The qualitative features of H_2 TPR profile obtained on pure ceria sample (Fig. 5a) are consistent with those reported by Giordano et al. [61] over a low surface area ceria sample following calcination in 20% O_2/He gas mixture at 773 K for 1 h. Similarly, the qualitative features of the H_2 TPR profile (based on the water signal) obtained on the present $Ce_{0.8}Zr_{0.2}O_2$ solid (Fig. 5b) are also in harmony with those obtained over the $Ce_{0.5}Zr_{0.5}O_2$ solid solution [62]. In the latter case, the first low-temperature TPR peak obtained in the present work (Fig. 5b) appeared as a shoulder of the rising part of the second TPR peak. This low-temperature TPR peak has also been observed on a $Ce_{0.68}Zr_{0.32}O_2$ solid solution [46].

The TPR profile of Fig. 5a shows that the kinetics of Ce(IV) reduction in CeO_2 is not much affected by the presence of $CePO_4$, while a slight influence is observed in the case of $Ce_{0.8}Zr_{0.2}O_2$ at high temperatures (a slight shift of peak maximum temperature). However, as Fig. 5 indicates, a part of the reducible oxygen species in the original Ce and CeZr samples is absent in the CeP and CeZrP phosphated solids. In particular, the first two TPR peaks of $Ce_{0.8}Zr_{0.2}O_2$ (CeZr) are completely absent in the CeZrP sample.

Considering the mechanism that is widely accepted for Ce(IV) reduction to Ce(III) [63], that of H activation, formation of new OH groups at the surface of the oxide (reversible reduction), water formation and desorption, and a surface O-vacancy formation (irreversible reduction), several pathways through which $CePO_4$ could influence the kinetics of reduction process might be proposed. First, the presence of $CePO_4$ can influence the reduction of surface Ce oxide because diffusion of O anions from the bulk to the surface is inhibited by the presence of $CePO_4$ in the surface/subsurface region of the solid (see also Scheme 1). The latter has been illustrated by the $^{18}O_2$ TPIE and transient isothermal experiments (Figs. 10 and 11) and it was previously discussed. Second, activation of hydrogen on the surface could be influenced by the presence of surface $CePO_4$ entities. Third, the presence of $CePO_4$ reduces the effective area for O diffusion from the bulk to the surface, as depicted in Scheme 1. This in turn reduces the rate of the surface reduction process.

Although the presence of $CePO_4$ has been detected in the phosphated Ce and CeZr solids, the possibility that a fraction of P could have been migrated into the inner bulk of the Ce oxide cannot be discarded. This inner P might worsen the bulk O-diffusion properties and, therefore, both the reducibility and the OSC properties of Ce and CeZr solids. In fact, it has been reported that P(V) ions can enter the fluorite CeO_2 structure and although their solubility can be only of a few percent of P_2O_5, the substitution of Ce(IV) with P(V) results in a reduction of the O-vacancy population [64]. The possibility that such a mechanism can operate and contribute to the deterioration of the OSC value of CeO_2 may not be discarded.

The present work has illustrated via the use of a number of different spectroscopic techniques, OSC measurements, and transient $^{18}O_2$ isotopic exchange experiments that the reducibility of Ce(IV) to Ce(III) and the related exchange of surface and bulk oxygen in CeO_2 and $Ce_{0.8}Zr_{0.2}O_2$ solids are negatively affected by the presence of surface and subsurface $CePO_4$. This finding appears to be significant for the current three-way catalytic technology because it is strongly related to the design of better oxygen-storage components than the currently used $Ce_{1-x}Zr_xO_2$ solid solutions. The rapid storage and release of oxygen derived from the fast oxygen chemisorption onto oxygen-vacant sites, and the subsequent surface and bulk diffusion processes of oxygen species, coupled with the quick response of Ce(IV)/Ce(III) redox pair, are at the heart of the current TWC technology. If $CePO_4$ predominates at the surface and in the subsurface region of $Ce_{1-x}Zr_xO_2$ solid, it is very likely that the OSC properties are irreversibly damaged because Ce(III) of $CePO_4$ is very stable and can be oxidized. Since $CePO_4$ has been found in

vehicle-aged TWCs [7,8], the results presented in this work strongly suggest that formation of $CePO_4$ must be considered as one of the main factors that determine the chemical deactivation of TWC.

5. Conclusions

The following conclusions can be derived from the results of the present work:

1. The amount of Ce(IV) that is reduced to Ce(III) at medium temperatures in a cubic $Ce_{0.8}Zr_{0.2}O_2$ solid solution is diminished by the deliberate addition of phosphorus in an amount $P/(Ce + Zr) = 0.2$ followed by calcination in air at 873 K for 12 h of the resulting solid.
2. Raman, XPS, and N_2 physical adsorption studies revealed that $CePO_4$ is present on the surface and in the subsurface region of CeO_2 and $Ce_{0.8}Zr_{0.2}O_2$ solids.
3. Oxygen-storage capacity measurements using H_2 and CO probe molecules have demonstrated the significant reduction of OSC quantity obtained in the phosphated CeO_2 and $Ce_{0.8}Zr_{0.2}O_2$ solids compared to those in the absence of phosphorus.
4. Various kinds of $^{18}O_2$ transient isothermal and temperature-programmed isotopic exchange experiments provided strong evidence that $CePO_4$ significantly reduces the specific rate of surface oxygen diffusion and that from the bulk to the surface of CeO_2 and $Ce_{0.8}Zr_{0.2}O_2$ solids.
5. The hypothesis that formation of $CePO_4$ on the surface and in the subsurface region of CeO_2 and $Ce_{0.8}Zr_{0.2}O_2$ solid crystals is one of the main chemical deactivation mechanisms of commercial three-way catalysts is strongly supported by the results of the present work.

Acknowledgments

The European Commission is gratefully acknowledged for funding the G5RD-CT-2000-00376 project under the 5th Framework Programme. The Regional Government of Madrid is also acknowledged for funding the 07M/0081/2002 project. F.C.G. also thanks the Spanish Ministry of Education and Culture for a doctoral fellowship.

References

[1] D.R. Liu, J.S. Park, Appl. Catal. B 2 (1993) 49.
[2] W.B. Williamson, J. Perry, H.S. Gandhi, J.L. Bomback, Appl. Catal. 15 (1985) 277.
[3] T.N. Angelidis, S.A. Sklavounos, Appl. Catal. A 133 (1995) 121.
[4] D.D. Beck, J.W. Sommers, C.L. Di Maggio, Appl. Catal. B 11 (1997) 257.
[5] D.E. Angove, N.W. Cant, Catal. Today 63 (2000) 371.
[6] M.J. Rokosz, A.E. Chen, C.K. Lowe-Ma, A.V. Kucherov, D. Benson, M.C.P. Peck, R.W. McCabe, Appl. Catal. B 33 (2001) 205.
[7] C. Larese, F.C. Galisteo, M.L. Granados, R. Mariscal, J.L.G. Fierro, M. Furió, R.F. Ruiz, Appl. Catal. B 40 (2003) 305.
[8] D. Uy, A.E. O'Neill, L. Xu, W.H. Weber, R.W. McCabe, Appl. Catal. B 41 (2003) 269.
[9] M. Tsuhako, S. Ikeuchi, T. Matsuo, I. Motooka, M. Kobayashi, Bull. Chem. Soc. Jpn. 52 (1975) 1034.
[10] M. Tsuhako, S. Ikeuchi, T. Matsuo, I. Motooka, M. Kobayashi, Chem. Lett. (1977) 195.
[11] R.G. Herman, A. Clearfield, J. Inorg. Nucl. Chem. 37 (1975) 1697.
[12] C. Larese, F.C. Galisteo, M.L. Granados, R. Mariscal, J.L.G. Fierro, P.S. Lambrou, A.M. Efstathiou, Appl. Catal. B 48 (2004) 113.
[13] R.M. Heck, R.J. Farrauto, Appl. Catal. A 221 (2001) 443.
[14] M. Shelef, R.W. McCabe, Catal. Today 62 (2000) 35.
[15] G. Smedler, S. Eriksson, M. Lindblad, H. Bernler, S. Lundgren, E. Jobson, SAE Technical Paper Series 930944 (1993).
[16] T.N. Angelidis, V.G. Papadakis, Appl. Catal. B 12 (1997) 193.
[17] U. Lassi, R. Polvinen, S. Suhonen, K. Kallinen, A. Savimäki, M. Härkönen, M. Valden, R.L. Keiski, Appl. Catal. B, in press.
[18] J. Kašpar, R. Di Monte, P. Fornasiero, M. Graziani, H. Bradshaw, C. Norman, Top. Catal. 16/17 (2001) 83.
[19] R.F. Ruiz, M. Furió, F.C. Galisteo, C. Larese, M.L. Granados, R. Mariscal, J.L.G. Fierro, Anal. Chem. 74 (2002) 5463.
[20] C.D. Wagner, L.E. Davis, M.V. Zeller, J.A. Taylor, R.H. Raymond, L.H. Gale, Surf. Interface Anal. 3 (1981) 211.
[21] H.C. Yao, Y.F. Yu Yao, J. Catal. 86 (1984) 254.
[22] C.N. Costa, T. Anastasiadou, A.M. Efstathiou, J. Catal. 194 (2000) 250.
[23] S. Bedrane, C. Descorme, D. Duprez, Catal. Today 75 (2002) 401.
[24] M. Yashima, K. Morimoto, N. Ishizawa, M. Yoshimura, J. Am. Ceram. Soc. 76 (1993) 2865.
[25] M. Yashima, H. Arashi, M. Kakihana, M. Yoshimura, J. Am. Ceram. Soc. 77 (1994) 1067.
[26] G. Colon, M. Pijolat, F. Valdivieso, H. Vidal, J. Kašpar, E. Finocchio, M. Daturi, C. Binet, J.C. Lavalley, R.T. Baker, S. Bernal, J. Chem. Soc., Faraday Trans. 94 (1998) 3717.
[27] J. Kašpar, P. Fornasiero, M. Graziani, Catal. Today 50 (1999) 285.
[28] J. Kašpar, P. Fornasiero, in: A. Trovarelli (Ed.), Catalysis by Ceria and Related Materials, Imperial College Press, London, 2002, p. 218.
[29] J.R. McBride, K.C. Hass, B.D. Poindexter, W.H. Weber, J. Appl. Phys. 76 (1994) 2435.
[30] J.E. Spanier, R.D. Robinson, F. Zheng, S.W. Chan, I.P. Herman, Phys. Rev. B 64 (2001) 24, 5407.
[31] W.H. Weber, K.C. Hass, J.R. McBride, Phys. Rev. B 48 (1993) 178.
[32] G. Vlaic, R. Di Monte, P. Fornasiero, E. Fonda, J. Kašpar, M. Graziani, J. Catal. 182 (1999) 378.
[33] G.A.H. Mekhemer, Colloids Surf. A 141 (1998) 227.
[34] A.A.M. Ali, M.I. Zaki, Thermochim. Acta 387 (2002) 29.
[35] P. Burroughs, A. Hamnett, A.F. Orchard, G. Thornton, Dalton (1976) 1686.
[36] D.R. Mullins, S.H. Overbury, D.R. Huntley, Surf. Sci. 409 (1998) 307.
[37] M. Romeo, K. Bak, J. El Fallah, F. Le Normand, L. Hilaire, Surf. Interface Anal. 20 (1993) 508.
[38] F.B. Noronha, E.C. Fendley, R.R. Soares, W.E. Alvarez, D.E. Resasco, Chem. Eng. J. 82 (2001) 21.
[39] A.E. Hughes, J.D. Gorman, P.J.K. Patterson, R. Carter, Surf. Interface Anal. 24 (1996) 634.
[40] A. Galtayries, R. Sporken, J. Riga, G. Blanchard, R. Caudano, J. Electron Spectrosc. Relat. Phenom. 88–91 (1998) 951.
[41] K. Bak, L. Hilaire, Appl. Surf. Sci. 70–71 (1993) 191.
[42] S.J. Gregg, K.S.W. Sing, Adsorption, Surface Area and Porosity, Academic Press, London, 1982.
[43] J. El Fallah, S. Boujana, H. Dexpert, A. Kiennemann, J. Majerus, O. Touret, F. Villain, F. Le Normand, J. Phys. Chem. 98 (1994) 5522.

[44] P. Fornasiero, T. Montini, M. Graziani, J. Kašpar, A.B. Hungria, A. Martinez-Arias, J.C. Conesa, Phys. Chem. Chem. Phys. 4 (2002) 149.
[45] M. Daturi, E. Finocchio, C. Binet, J.C. Lavalley, F. Fally, V. Perrichon, H. Vidal, N. Hickey, J. Kašpar, J. Phys. Chem. B 104 (2000) 9186.
[46] H. Vidal, S. Bernal, J. Kašpar, M. Pijolat, V. Perrichon, G. Blanco, J.M. Pintado, R.T. Baker, G. Colon, F. Fally, Catal. Today 54 (1999) 93.
[47] N. Hickey, P. Fornasiero, R. Di Monte, J. Kašpar, M. Graziani, G. Dolcetti, Catal. Lett. 72 (2001) 45.
[48] S. Rossignol, F. Gérard, D. Duprez, J. Mater. Chem. 9 (1999) 1615.
[49] Y. Madier, C. Descorme, A.M. Le Govic, D. Duprez, J. Phys. Chem. B 103 (1999) 10999.
[50] G.K. Boreskov, Adv. Catal. 15 (1964) 285.
[51] K. Klier, J. Novakova, P. Jiru, J. Catal. 2 (1963) 479.
[52] D. Martin, D. Duprez, J. Phys. Chem. 100 (1996) 9429.
[53] C. Descorme, Y. Madier, D. Duprez, J. Catal. 196 (2000) 167.
[54] M. Che, A.J. Tench, Adv. Catal. 32 (1983) 1.
[55] P. Meriaudeau, J.C. Vedrine, J. Chem. Soc., Faraday Trans. 72 (1976) 472.
[56] J. Cunningham, E.L. Goold, J.L.G. Fierro, J. Chem. Soc., Faraday Trans. 78 (1982) 785.
[57] K.P. Peil, J.G. Goodwin, G. Marcelin, J. Catal. 131 (1991) 143.
[58] P. Vidmar, P. Fornasiero, J. Kašpar, G. Gubitosa, M. Graziani, J. Catal. 171 (1997) 160.
[59] C. Janvier, M. Pijolat, F. Valdivieso, M. Soustelle, Solid States Ionics 127 (2000) 207.
[60] M. Che, A.J. Tench, Adv. Catal. 31 (1982) 77.
[61] F. Giordano, A. Trovarelli, C. de Leitenburg, M. Giona, J. Catal. 193 (2000) 273.
[62] P. Fornasiero, J. Kašpar, M. Graziani, Appl. Catal. B 22 (1999) L11.
[63] S. Bernal, J.J. Calvino, G.A. Cifredo, J.M. Rodriguez-Izquierdo, J. Phys. Chem. 99 (1995) 11794.
[64] M. Boaro, A. Trovarelli, J.H. Hwang, T.O. Mason, Solid State Ionics 147 (2002) 85.